

Correlation of optical attenuation coefficient estimated using optical coherence tomography with changes in astrocytes and neurons in a chronic photothrombosis stroke model

SHANSHAN YANG,¹ KEZHOU LIU,^{3,5} LIN YAO,¹ KAIYUAN LIU,¹
GUOQING WENG,⁵ KEDI XU,^{2,3,4,6} AND PENG LI^{1,7} 

¹State Key Lab of Modern Optical Instrumentation, College of Optical Science and Engineering, Zhejiang University, Hangzhou, Zhejiang 310027, China

²Qiushi Academy for Advanced Studies (QAAS), Zhejiang University, Hangzhou, Zhejiang 310027, China

³Department of Biomedical Engineering, Key Laboratory of Biomedical Engineering of Education Ministry, Zhejiang University, Hangzhou, Zhejiang 310027, China

⁴Zhejiang Provincial Key Laboratory of Cardio-Cerebral Vascular Detection Technology and Medicinal Effectiveness Appraisal, Zhejiang University, Hangzhou, Zhejiang 310027, China

⁵College of Artificial Intelligence, Dept. of Biomedical Engineering, Hangzhou Dianzi University, Hangzhou, Zhejiang 310018, China

⁶xukd@zju.edu.cn

⁷peng_li@zju.edu.cn

Abstract: The optical attenuation coefficient (OAC) estimated using optical coherence tomography (OAC-OCT) offers a label-free 3D mapping of tissue infarction, but the physiological origin of the OAC contrast remains unclear. For effectively suppressing OAC fluctuations, we propose a hybrid (wavelength/angle) division multiplexing (HDM) method, which improved the OAC contrast by 70.7% in tissue phantoms. To test the feasibility of OAC-based infarction detection, triphenyltetrazolium chloride (TTC) staining was performed on fresh *ex vivo* brain slices, and the TTC-defined infarction was used as the ground truth. Sharp OAC contrast was observed between the TTC-defined infarction (1.09 mm^{-1}) and normal tissue (0.79 mm^{-1}). The OAC infarction spatially matched well with the TTC-defined infarction. To further explore the physiological origin of OAC contrast in ischemic stroke at the cellular level, the dynamic changes in OAC were measured in the rat cortex *in vivo* over 3 weeks after photothrombosis (PT) occlusion and found significantly correlated with the changes in astrocytes and neurons acquired with *ex vivo* hematoxylin and eosin (HE), glial fibrillary acidic protein (GFAP), and NeuN staining. These results suggest that OAC imaging enables non-invasive infarction detection and its contrast might originate from the changes in astrocytes and neurons in the chronic PT stroke model. The cellular responses revealed by *in vivo* OAC imaging would be essential for evaluating treatments and even developing novel therapies.

© 2019 Optical Society of America under the terms of the [OSA Open Access Publishing Agreement](#)

1. Introduction

Focal ischemic stroke begins with the blockage of cerebral blood vessels in a certain brain region. Ischemia causes cell death and brain-tissue damage in the core area, and induces a series of endogenous vascular and cellular alterations in the penumbra [1]. Therefore, the evaluation of vascular and cellular responses to ischemic stroke is crucial to understand the mechanism of neurovascular coupling and brain-tissue response. Optical coherence tomography (OCT) imaging creates multiple images with endogenous contrast by using the intrinsic optical scattering properties of red blood cells and brain tissues, and it is a label-free, non-invasive, three-dimensional, and real-time method to monitor vascular and cellular responses [2–4].

OCT angiography (OCTA) and optical attenuation coefficient (OAC) imaging allow the multi-parametric evaluation of experimental ischemic stroke [2,5,6], with parameters including capillary perfusion, cerebral blood flow, and cellular scattering. It was found that the OAC correlates to the degeneration of brain tissue in ischemic stroke and offers a label-free 3D mapping of tissue infarction [2,5–7].

OAC contrast imaging of injured tissues requires precise OAC measurement. OAC measurement is initially performed by fitting an exponential curve through the OCT depth profile [8–11], which is time-consuming and requires tissue with a relatively uniform attenuation coefficient within a certain depth range. Recently, Vermeer *et al.* developed a method based on a single scattering model to determine depth-resolved OACs from OCT depth profiles [12]. The mapping of localized, per-pixel OACs enables the comprehensive interpretation of optical-property changes in heterogeneous multi-layered tissues such as the cerebral cortex. Although each pixel in the OCT depth profiles can be converted into a corresponding pixel in the OAC image, a single measurement exhibits great fluctuation, most likely because of system and speckle noise as well as tissue heterogeneity [13,14]. The fluctuation in OAC measurement poses a great challenge to OAC-based threshold segmentation [14]. Ideally, OACs of two different tissue classes should have a bimodal histogram without overlap, but in practice, the fluctuation makes the OAC histograms spread with a large overlap, resulting in serious segmentation errors [15]. The usual approach to improve the histogram shape is averaging with a spatial kernel [10,16]. Effective averaging requires completely independent samples. However, most samples within the spatial kernel normally have a spatial overlap and corresponding residual correlation, resulting in an inferior averaging performance for sharpening the OAC histogram. Thus, an effective averaging method is desired to suppress the fluctuations in OAC measurement and to improve the OAC-based image segmentation.

The interpretation of OAC results requires a thorough understanding of the physiological origin of OAC contrast. Choi *et al.* reported that OAC changes are spatially correlated to infarct tissues in the distal middle cerebral artery occlusion model of a mouse and might reveal the pathogenesis of tissue infarction and penumbra development in the acute phase (from minutes to hours) of ischemic stroke [5]. The acute phase (approximately the first 3 h after the onset of occlusion) is a critical therapeutic window for thrombolytic treatment to rescue penumbra, but the majority of patients fail to receive treatment in time because the window is too narrow [17]. As an important alternative, neurorestorative therapy aims to maximize the neural function of the surviving brain in the chronic phase (days post occlusion) [18,19]. By using a rat chronic photothrombosis (PT) stroke model (2 weeks), the dynamic change in cellular scattering has been observed in our previous study [6]. Although it was assumed that OAC changes were caused by the destruction of cellular integrity and function in ischemic stroke, the physiological origin of ischemia-induced OAC changes remains unknown in the acute phase as well as the chronic phase, severely hindering the appropriate interpretation of OAC results.

In this study, we propose a hybrid (wavelength/angle) division multiplexing (HDM) method for high-precision OAC measurement and validate its performance by using tissue phantoms (TPs). The feasibility of OAC infarction detection was tested experimentally by comparison with triphenyltetrazolium chloride (TTC)-defined infarction in *ex vivo* brain slices from a rat PT stroke model. Furthermore, longitudinal monitoring was performed over three weeks on the rat cortex *in vivo* pre and post stroke with OAC and OCTA. We found that OAC measurement spatiotemporally correlated to the results of histological and immunohistological staining, including hematoxylin-eosin (HE), glial fibrillary acidic protein (GFAP), and NeuN staining. This result suggested that OAC imaging enables non-invasive infarction detection and that its contrast might originate from the changes in astrocytes and neurons in the chronic PT stroke model. The cellular responses revealed by *in vivo* OAC imaging are expected to be essential for evaluating treatments and even developing novel therapies.

2. Methods

2.1. OCT system and signal processing

A lab-built OCT system was used for *in vivo* and *ex vivo* imaging of the rat cerebral cortex. The OCT system, which is primarily based on a typical spectral domain configuration, has been specified in Ref. [6]. In brief, a broadband super-luminescent diode (SLD) with a central wavelength of 1325 nm and half-maximum bandwidth of 100 nm was used as the light source, yielding a measured axial (depth) resolution of 7.6 μm in air. The probing light was focused onto the brain tissue with an objective lens (focal length = 36 mm), and a lateral resolution of 10 μm was achieved. Spectral interference fringes were recorded with a customized high-speed spectrometer equipped with a fast line-scan InGaAs camera (120-kHz line-scan rate). The system sensitivity was measured at ~98 dB with 3-mW light on the sample, and the system exhibited a roll-off of ~6 dB at a depth of ~1.5 mm. The sensitivity roll-off is caused by the limited spectral resolution. Assuming a Gaussian spectral resolution, the Fourier transform generates a Gaussian-shaped sensitivity roll-off factor, which can be estimated by fitting the recorded sensitivity roll-off curve.

A stepwise raster scanning protocol was adopted to acquire volumetric datasets (z - x - y). Along the x direction (the fast scan axis), 512 A-lines formed a B-frame, and 2560 B-frames were captured in total at 512 y -locations (the slow scan axis) with 5 repeated B-frames at each y -location. Each 3D data set took a total acquisition time of ~13.4 s and covered a cortical surface area of 3 mm by 3 mm, corresponding to a raw-data cube of the spectral interferogram $S(k, x, y, t)$, where k is the wavenumber and t is the index of the repeated B-frames. Fast Fourier transform was performed on the raw spectral interference fringe signal $S(k, x, y, t)$ along the direction of the wavenumber k to generate the reflectivity profile $A(x, y, t)$ in the depth (z) space. The intensity $I(z, x, y, t)$, i.e., the modulus of $A(z, x, y, t)$, was used to generate the structural cross-section.

OAC estimation. Incident light is exponentially attenuated along its propagation path in turbid tissues because of the scattering and absorption of light. The OAC is an intrinsic optical property of bio-tissues that reveals valuable information on tissue composition. The OCT depth profile offers an effective approach to estimate tissue OAC. The localized, per-pixel OAC was measured as follows [12]:

$$\mu_z \approx \frac{I_z}{2\Delta \sum_{z+1}^{\infty} I_z}, \quad (1)$$

where μ_z and I_z denote the attenuation coefficient and signal intensity of the z^{th} pixel along the OCT A-line, respectively, and Δ denotes the pixel size in the depth direction. Thus, a depth-resolved mapping of tissue OAC can be obtained. In low-NA optics, the sensitivity roll-off would be the main factor affecting the OAC calculation [20]. Thus, each A-line was divided by the roll-off factor before the OAC calculation [5]. Typically, averaging was performed with a spatial kernel for smoothing the OAC measurement [10], but the smoothing performance was limited by the spatial dependence within the kernel. In the present study, an HDM method was developed for high-precision OAC measurement with a wavelength-angle kernel. In the method, independent samples were generated by splitting the wavelength spectrum [5,21] and the full-space B-scan modulation spectrum [22] with a set of Gaussian filters, which were initially proposed for enhancing the flow contrast in OCTA. The splitting numbers of the wavelength spectrum and the full-space B-scan modulation spectrum were both set as 5 in the present study, and a total of 5×5 OAC sub-images were generated and compounded for the resultant cross-sectional OAC mapping. The center positions of the Gaussian filters were evenly spaced (an interval of 20% of the full spectrum) across the spectrum regions with a constant bandwidths of 23% to ensure a full use of the original signals, resulting in a $4.3\times$ degradation of the spatial resolution in the sub-images (i.e. ~33 μm and 43 μm in the axial and lateral directions, respectively).

OCTA. To visualize blood perfusion within the tissue bed, OCTA was achieved by analyzing the temporal dynamics between repeated B-frames. The inter-frame decorrelation of $A(z, x, y, t)$ was computed based on complex OCT signals, which enables higher motion sensitivity because of the comprehensive utilization of amplitude and phase information. In addition, to suppress noise-induced decorrelation artifacts, the inverse signal-to-noise ratio (iSNR)-decorrelation OCTA (ID-OCTA) algorithm was applied to remove static and noise regions at all SNRs in intensity-decorrelation feature space [23].

2.2. Animal preparation and PT ischemia model

Eight groups of adult male Sprague-Dawley rats (10 weeks old, weighing 300–330 g) were used in this study (Table 1). All rats were obtained from Zhejiang Medical Science Institute (Grade II, Certification No. SCXK2003-0001), and all animal experimental procedures in this study were in accordance with the guidelines for the care and use of laboratory animals of the Chinese Ministry of Health and approved by Zhejiang University Animal Care and Use Committee. Animal preparation, the assembly of a long-lasting optical window, and PT vascular occlusion were performed using procedures similar to those previously described [6]. Briefly, the rat was anesthetized with pentobarbital sodium (1%, 50 mg/kg) and fixed in a stereotaxic apparatus (C6V06-001, RWD Life Science Ltd., China). A 4 mm by 4 mm craniotomy was performed with the center at 4.5 mm posterior and 2 mm lateral to bregma by using a dental drill (STRONG90, RWD Life Science Ltd., China). The skull and dura were carefully detached using fine forceps and replaced with a transparent glass coverslip. Methyl methacrylate acrylic resin (Vertex-Dental, Netherlands) was used to seal the glass coverslip to the skull, yielding a flat tissue surface as an imaging window. After the rats recovered from the initial optical-window surgery, PT occlusion was administrated in the ischemic rats with 30-min laser illumination over the region of interest (ROI) within the cortical window. During OCT imaging, the probing beam was directed for oblique incidence on the tissue surface to avoid specular reflections. The lower boundary of the glass coverslip was demarcated automatically. According to the boundary information, the air and glass parts (above the boundary) were completely removed from the images, and the brain tissue (below the boundary) was flattened before calculating the OAC and before generating the OCT/OCTA images.

Table 1. Groups of rats used for optical imaging of the cortex, imaging times, and methods of imaging. Days 1–21 indicate the day post PT occlusion. All the rats were male and 10 weeks old.

Group	#1	#2	#3	#4	#5	#6	#7	#8
Number of Rats	5	8	5	5	5	5	5	5
Time Points	Day 3	Every day	Baseline	Day 1	Day 3	Day 7	Day 14	Day 21
Imaging	TTC and OCT		OCT		HE, GFAP, and NeuN			

OCT imaging and TTC staining. Rats in Group #1 were sacrificed on Day 3 after PT for TTC staining and *ex vivo* OAC-OCT imaging. On Day 3 after PT, the rats were euthanized, and their brains were isolated and sliced rostro-caudally into serial 2-mm-thick slices. The brain slices were incubated in 2% TTC for 30 min at 37 °C and subsequently imaged with a microscope (Olympus, SZ3060) and OAC-OCT within 5 min. Using TTC as a redox indicator, viable tissues become red, while non-viable infarct stays in their original white color [24]. The boundary of the infarction region was delineated using image-analysis software (OSIRIS 4.19; Geneva, Switzerland) based on the obtained image. The structural and OAC projections were generated by averaging over a depth range from the surface to a depth of 500 μm . And the image of whole brain slice was generated by stitching together 24 images of size 3 mm by 3 mm. By using the TTC boundary as the ground truth, the OAC threshold was determined for infarction detection by maximizing the specificity under the condition of 100% sensitivity. The specificity

is the proportion of normal tissue (i.e., negative examples) that is correctly rejected, while the sensitivity is defined as the proportion of damaged tissue (i.e., positive examples) that is correctly identified. The condition of 100% sensitivity was adopted to ensure that the damaged tissue is completely identified. On Day 3, the rats exhibit the largest damaged area, covering the ischemic core and penumbra. Therefore, the data of Day 3 are the most representative for determining the OAC threshold.

OCT imaging, HE staining, and immunostaining. The rats in Group #2 were imaged with OCT at baseline (before PT), 1 h after PT stroke, and subsequently every day over 3 weeks *in vivo*. The changes in tissue scattering and vasculature in response to focal ischemia were revealed with OAC-OCT and OCTA by analyzing the depth profiles and temporal dynamics of the intrinsic backscattered light, respectively. Six groups of rats (Group #3–8) were transcardially perfused without PT (baseline, Group #3) as well as 1 h, 3 days, 7 days, 14 days, and 21 days after PT (Group #4–8) for histological and immunohistochemistry staining, respectively. The rats were anesthetized with chloral hydrate (10%, 4 mL/kg) and transcardially perfused first with ice-cold phosphate-buffered saline (PBS) and subsequently with 4% paraformaldehyde [25]. After perfusion, the brain was post-fixed with 4% paraformaldehyde. Coronal sections of the brain (thickness of 10 μm) were cut using a cryostat (Leica CM 1900) and then collected serially on precleaned slides. Generally, three slices with the maximum damage area were selected for analysis. In the statistical analysis of infarction area and cellular density, the selected slices of each rat brain were averaged as one value, and the values from five rats in each group were averaged as the group value (Group #3–8).

Estimation of infarct area. To estimate the spatio-temporal evolution of the infarction area, coronary brain slices (Group #3–8) were stained using 10% hematoxylin and 0.5% eosin. The sections were imaged using a bright-field microscope (Olympus, BX61). The infarction area was delineated using the image-analysis software OSIRIS 4.19, and the infarction area A_{HE} was quantified at each time point. The criteria used to determine brain-cell damage were similar to those used by Watanabe *et al.* [26]. Briefly, if the area consisted of a majority of either eosinophilic neurons or ghost neurons with no nucleus and the loss of all cellular detail (coagulative necrosis) or cavitation with neuronal loss, these areas were defined as damaged tissue. The *en-face* OAC mapping was generated by averaging the OAC within a depth range of 0–500 μm beneath the cortical surface, mainly including the cortex layer 2/3, which has abundant neurons [27,28]. By using the selected OAC threshold, the area of the elevated-OAC region A_{OAC} was obtained by calculating the product of the single-pixel size and number of pixels within the region.

Estimation of GFAP+ and NeuN+ cell density. Immunostaining was performed to assess the dynamic changes in astrocytes and neurons separately. Brain slices were incubated with rabbit polyclonal anti-GFAP (BA0056, 1:50, Boster) overnight, and the astrocytes were stained in brown. Rabbit anti-NeuN (ab177487, 1:50, Abcam) antibody was used for neuron detection, and the neuron nuclei were stained in brown or dark brown. Considering that the distributions of astrocytes and neurons are spatiotemporally dependent, GFAP+ and NeuN+ cells were counted in small ROIs of $200 \times 200 \mu\text{m}^2$ in layer 2/3 in three typical regions: the ischemic core area (IC), core-penumbra boundary (CP boundary), and reversible penumbra (RP) outside the ischemic core. For non-ischemic rats (Group #3), cells were counted in the equivalent region of the same size. The OAC values from OAC cross-sections were also measured and averaged within the group (Group #2) in 3 ROIs, including IC (OAC increased without recovery on Day 21), RP (OAC increased and then recovered on Day 21), and the CP boundary (between IC and RP), from the OAC projections. Averaging was performed to reduce the fluctuation in quantification.

2.3. Statistical analysis

Quantitative data were expressed as mean \pm standard deviation (Std). Welch's t-test was performed to calculate the significance of the differences between the OAC values of the TTC-defined infarction and the normal tissue. $p < 0.05$ was considered statistically significant.

3. Results

3.1. Precise OAC measurement based on HDM with low variance in tissue phantoms

Figure 1(a) shows a representative cross-section of the TPs, which had two different preparation ratios (TP1: 1% agar and 5% lipid; TP2: 1% agar and 10% lipid). The OCT depth profile (the curve on the left in Fig. 1(a) revealed the decay of the received OCT signal along the depth direction, and the depth-resolved OAC was derived from the intensity attenuation against depth. Figure 1(b) shows cross-sectional OAC images of the yellow rectangular region in Fig. 1(a) without (upper panel) and with (lower panel) the HDM method. The HDM method yielded smooth contrast with less fluctuations and a sharp boundary of the phantoms TP1 and TP2 (see the yellow arrows). As shown by the OAC histograms in Fig. 1(c), the HDM method yielded more concentrated histogram distributions (i.e., smooth contrast and less fluctuations in Fig. 1(b)) in both ROI1 (Mean \pm Std: $0.44 \pm 0.04 \text{ mm}^{-1}$) and ROI2 (Mean \pm Std: $0.67 \pm 0.10 \text{ mm}^{-1}$) compared with the original images (ROI1, Mean \pm Std: $0.47 \pm 0.19 \text{ mm}^{-1}$; ROI2, Mean \pm Std: $0.69 \pm 0.26 \text{ mm}^{-1}$). Furthermore, the HDM method resulted in a deep valley in the histograms and superior separability, as evidenced by the sharp boundary in Fig. 1(b). The separability score, defined as $S = |Mean_1 - Mean_2| / (Std_1 + Std_2)$, can be calculated between ROI1 and ROI2, where $Mean_1$ and Std_1 are the mean value and Std in ROI1, respectively, and $Mean_2$ and Std_2 are the mean value and Std in ROI2, respectively. As shown in Fig. 1(d), the HDM method yielded a maximal separability of 1.67 at an averaging number of $N = 25$, which corresponds to an improvement of 70.7% over that of spatial averaging.

3.2. Comparison of OAC-detected infarction and TTC-defined infarction in fresh *ex vivo* brain slice

As shown in Fig. 2(a), the infarction (hollow arrow) was clearly visualized with TTC staining in the representative fresh *ex vivo* brain slice (Day 3 post PT) in Group #1. By zooming in on the rectangular region of Fig. 2(a) (see the upper panel in Fig. 2(d)), the boundary of the ischemic region has been demarcated with blue dashed lines. In the structural projection of the coronal slice shown in Fig. 2(b), the infarction and normal tissues are not clearly distinguished. In contrast, the OAC projection image in Fig. 2(c) presented sharp contrast with enhanced visibility of the ischemic region. The OAC ischemic region was zoomed in (see the lower panel in Fig. 2d) and spatially co-registered with the TTC image. With the guidance of the TTC boundaries (blue dashed lines), two small regions of the same size (red: ischemic tissues; green: normal tissues) were selected from the OAC images for histogram analysis (see Fig. 2(e)). The HDM method yielded an obvious valley in the OAC histograms of the ischemic (Mean \pm Std: $1.09 \pm 0.07 \text{ mm}^{-1}$) and normal tissues (Mean \pm Std: $0.79 \pm 0.08 \text{ mm}^{-1}$), indicating a high separability score of 1.89 between ischemia and normal tissues in the PT stroke model. According to the OAC measurement of the 5 rats in Group #1, the OAC values for the TTC-defined infarction was significantly different from the values for the normal tissue in Welch's t-test ($p = 0.003$). By using the TTC boundaries as the ground truth, a maximal sensitivity of 100% and a specificity of 83.8% were achieved with an OAC threshold of 0.90 mm^{-1} (see Fig. 2(f)). The OAC-threshold-generated boundaries (the yellow lines in Fig. 2(d)) matched well with the TTC-defined infarction boundaries.

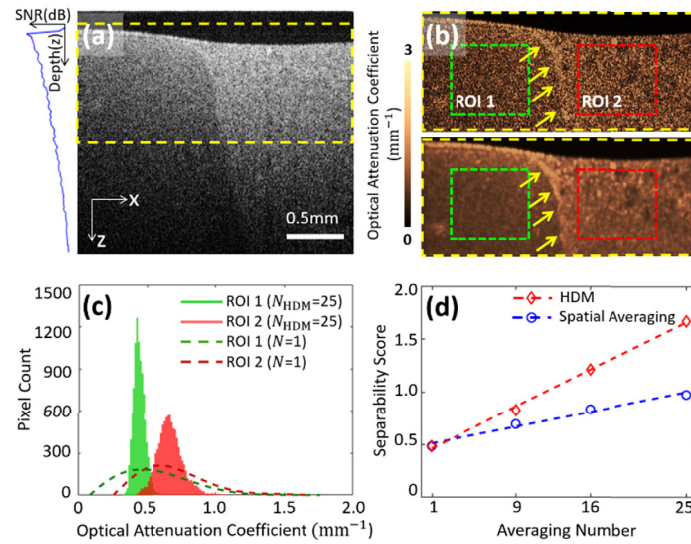


Fig. 1. Hybrid division multiplexing (HDM) enables enhanced separability in tissue phantoms (TPs) with different optical attenuation coefficients (OACs). (a) Representative cross-section of TP1 and TP2. TP1 is the left part, which consists of 1% agar and 5% intralipid, while TP2 is the right part, which consists of 1% agar and 10% intralipid. The curve on the left shows the averaged OCT depth profile, indicating the signal decay. (b) Cross-sectional OAC mappings of the rectangular region in (a) without (upper panel) and with (lower panel) the HDM method. $N = 25$. The arrows indicate the boundary between TP1 and TP2. (c) OAC histograms of regions of interest (ROI1 and ROI2) with (bars) and without (dashed lines) the HDM method. ROI1 and ROI2 were selected from TP1 and TP2, respectively, in Fig. 1b. (d) Measured separability scores and fitting lines of the spatial averaging method and HDM method with different kernel sizes.

3.3. In vivo OAC mapping in PT stroke model

Serial OCT imaging was performed on the rat cortex (Group #2; $n = 8$) every day for three weeks after PT. As shown in the *en-face* OAC maps (see the upper panel in Fig. 3(a) of a rat in Group #2, an elevated-OAC region was observed immediately after PT stroke (Day 1, compared with baseline). The elevated-OAC region expanded in the first 3 days and subsequently diminished. The red circled line in Fig. 3f plot the dynamic change of the area of the elevated-OAC regions A_{OAC} . The area A_{OAC} increased from Day 1 ($2.18 \pm 0.35 \text{ mm}^2$) after ischemia and reached a maximum on Day 3 ($4.56 \pm 0.41 \text{ mm}^2$); subsequently, it gradually diminished till the end of the study ($1.83 \pm 0.30 \text{ mm}^2$ on Day 21). According to the OAC projection images, the IC (the red dashed curve in Fig. 2(a) and RP (the annular ring between the green and red dashed curves in Fig. 2(a) were demarcated, and the CP boundary was between IC and RP. The corresponding time sequences of the cross-sectional OAC images are also shown in Fig. 3(a) (lower panel). In the cross-sections, the OAC changes in three typical regions (IC, CP boundary, and RP) were calculated (see the red circled lines in Fig. 3(g)–(i)). In IC, OAC increased on Day 1 after PT and quickly decreased in the subsequent days (see the red circled lines in Fig. 3(g)). In CP boundary, OAC increased continuously after PT (see the red circled line in Fig. 3(h)). In RP, OAC increased and reached a peak value on Day 3 after PT and gradually decreased thereafter (see the red circled line in Fig. 3(i)).

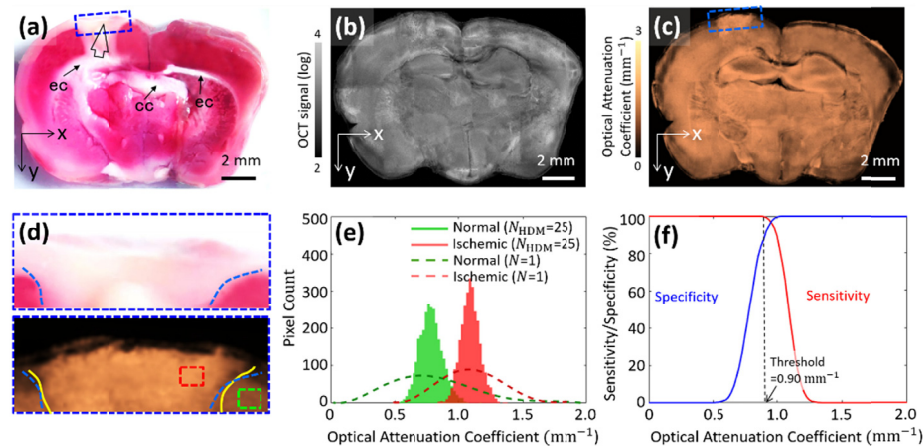


Fig. 2. Validation of infarction detection using OAC-OCT through a fresh *ex vivo* brain slice with TTC staining. (a) Coronal brain slice with TTC staining. The hollow arrow indicates focal PT infarction (ec: external capsule; cc: corpus callosum). (b) OCT structural projection view of the coronal slice. (c) Projection image of OAC with the proposed HDM method. (d) Enlarged views of the rectangular region in (a) and (c). Blue dotted lines and yellow lines indicate the boundaries of the TTC- and OAC-defined infarction, respectively. (e) OAC histograms of the selected infarct (red box in (d)) and normal (green box in (d)) regions with ($N_{HDM}=25$) and without ($N=1$) the HDM method. (f) Diagnostic sensitivity (red) and specificity (blue) of using OAC with the HDM method ($N_{HDM}=25$). A threshold of 0.90 mm^{-1} (see the black dashed line) yielded a sensitivity of 100% and a specificity of 83.8%. The large field-of-view in (b) and (c) was achieved by stitching together 24 images of size 3 mm by 3 mm. Both the structural and OAC projections were generated by averaging over a depth range from the surface to a depth of 500 μm .

3.4. Spatial correspondence of *in vivo* OAC mapping with OCTA ischemic region in PT stroke

The spatiotemporal evolution of the ischemic regions was revealed with OCTA *in vivo*. Figure 3(b) (upper panel) shows the *en-face* OCT angiograms of the representative time sequences for one rat before (baseline) and after occlusion (Day 1–21). In the baseline, the distal middle cerebral arteries (dMCAs), pial microvessels, and cortical capillary bed were observed clearly. The blood-flow signal disappeared in the focal ischemic region (see the yellow circle for Day 1) after 30-min laser irradiation. In the 3 subsequent days, the focal ischemic region spread with obvious disappearance of the capillary network outside the irradiation core (see the yellow dotted curve for Day 3). In Day 7–21, blood perfusion reappeared in the superficial layer of the ischemic area. The area of the non-perfusion region was quantified at each time point (see the pink squared line in Fig. 3(f)), and it reached the maximum on Day 3 after PT, which is consistent with the OAC series (see the red circled line in Fig. 3(f)). In the depth direction, Fig. 3(b) (lower panel) shows the time sequences of the cross-sectional OCT angiograms along the dashed line (across the center of the ischemia area). A non-perfusion area was observed on Day 1 and Day 3 (see the yellow rectangle for Day 1), which gradually disappeared in Day 7–21. Accordingly, serial OCT angiograms validated the PT stroke model and presented the spatiotemporal changes of the ischemic area.

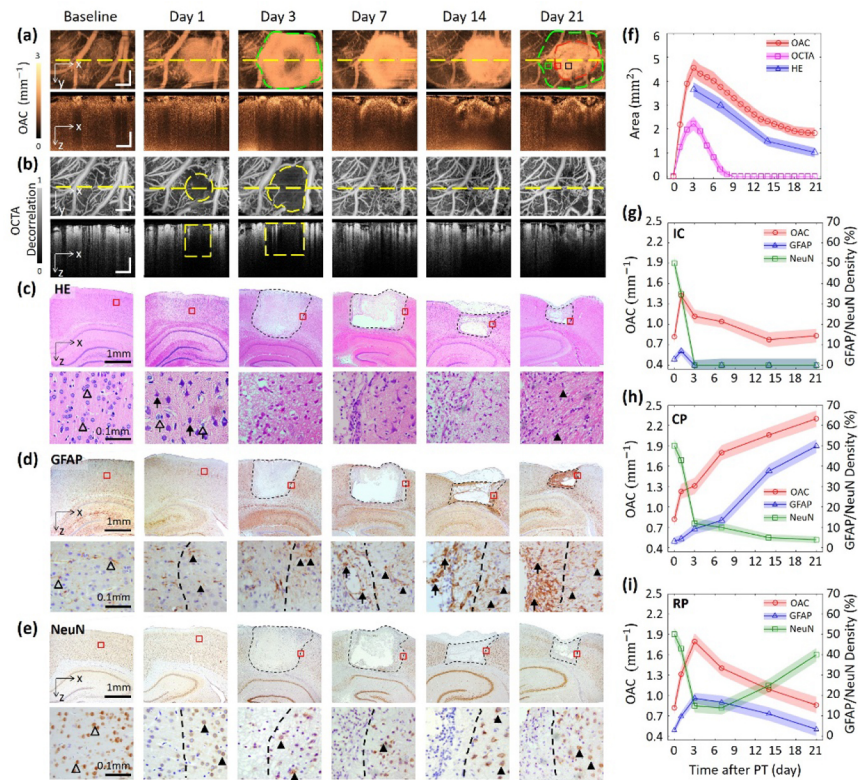


Fig. 3. Correlation of the Optical attenuation coefficient (OAC) with the changes in blood perfusion and histology in the photothrombosis (PT) stroke model *in vivo*. (a) Representative OAC time sequences. Upper panel: OAC projection maps (x-y). Ischemia core (IC): the red dashed curve; the reversible penumbra (RP): the annular ring between the green and red dashed curves; the ischemia core and penumbra (CP) boundary: the boundary between IC and RP. Lower panel: Corresponding OAC cross-sections (x-z) along the yellow dashed line. (b) Representative OCTA time sequences. Upper panel: OCTA maps (x-y). The yellow circle for Day 1 marks the ischemia area caused by laser irradiation, and the dotted curve for Day 3 marks the expanded ischemic area. Lower panel: Corresponding OCTA cross-sections (x-z) along the yellow dashed line. (c) Representative HE time sequences. Upper panel: brain slices with HE staining (6 rats). Lower panel: Corresponding enlarged views of 6 ROIs from the damage boundary in the upper panel. The black dashed line traces the boundary of the damaged area according to HE staining. The hollow arrowheads mark normal neurons with a large round nucleus and prominent nucleoli in the baseline. The solid arrows mark apoptotic neurons, and hollow arrows marked edema and shrunken nuclei in the infarction area. The solid arrowheads mark neurons with normal morphological features around the infarction area. (d) Representative GFAP time sequences. Upper panel: Corresponding GFAP immunostaining sections (6 rats). The dashed lines represent boundaries drawn according to GFAP+ cells. Lower panel: Enlarged views of 6 ROIs from the damage boundary in the upper panel. The black dashed lines represent the boundary of the damaged area according to GFAP+ cells, and the hollow and solid arrowheads are astrocyte examples in the undamaged area and around the damaged region. The solid arrows are astrocyte examples appearing in the damaged area, which formed astroglial scar tissue. (e) Representative NeuN time sequences. Upper panel: Corresponding NeuN immunostaining sections (6 rats). The dashed lines represent boundaries drawn according to NeuN+ cells. Lower panel: Corresponding enlarged view of 6 ROIs from the damage boundary in the upper panel. The black dashed line represents the boundary of the infarcted region, and the hollow and solid arrowheads indicate normal neurons in the undamaged area. (f) Measurement of ischemic or damaged areas based on blood perfusion (pink squares), OAC (red circles), and HE staining (blue triangles). (g-i) Measurement of the OAC (red circles) and the density of GFAP+ (blue triangles) and NeuN+ (green squares) cells in IC (g), the CP boundary (h), and RP (i) over time after PT. Scale bar = 500 μm .

3.5. Correlation of OAC mapping with ischemic infarction by HE staining in PT

The spatiotemporal evolution of the ischemic infarction areas was further acquired with HE staining before and after PT stroke (Group #3–8), as shown in Fig. 3(c). The normal neurons were observed with large and plump nuclei (see the hollow arrowheads at the baseline in Fig. 3(c)). Apoptotic neurons with condensed nuclei (see the solid arrows in Fig. 3(c)) and edema with widened intercellular spaces (see the hollow arrows in Fig. 3(c)) were observed 1 h post PT, which is consistent with previous reports [29,30]. The lesions were discernible in the first day after PT but with no obvious boundary, which was most likely due to the fact that the complete phagocytosis of dead or apoptotic neurons takes 2–3 days. On Day 3 after PT, no normal neuron was observed in the lesion area, and the dashed lines indicate the ischemic infarction boundary (see Day 3–21 in Fig. 3(c)). Along with the recovery of the infarction region, neurons with normal morphology appeared near the infarction area (see the solid arrowheads in Fig. 3(c)). The triangle curve in Fig. 3(f) plots the dynamic change of the HE infarction area A_{HE} . The infarction area increased and reached the maximum ($3.84 \pm 0.39 \text{ mm}^2$) on Day 3 after ischemia and then gradually reduced ($0.96 \pm 0.30 \text{ mm}^2$ at Day 21), suggesting delayed infarction expansion and spontaneous recovery after ischemic brain injury. The HE infarction area A_{HE} was spatiotemporally correlated to the OAC-elevated area A_{OAC} with a Pearson correlation coefficient of up to 97% (see Fig. 3(f)).

3.6. Correlation of OAC mapping with astrocyte response to PT by GFAP staining

In the normal rat cortex, the astrocytes exhibited a stellate morphology with low GFAP expression (see the hollow arrowheads at the baseline in Fig. 3(d)). After PT stroke, enhanced GFAP expression was observed, and GFAP+ astrocytes were densely packed on the boundary of the ischemic area, forming a stream with their elongated processes pointing towards the ischemic core. The GFAP+ astrocytes finally formed astroglial scar tissue (see the solid arrows for Day 7–21 in Fig. 3(d)). The astrocytes in the distant regions from the penumbra had a morphology and density similar to those of the astrocytes in the baseline (see the solid arrowheads for Day 1–21 in Fig. 3(d)). According to the GFAP+ astrocyte density, experienced experimentalists manually demarcated the boundaries of the ischemic lesion (see the dashed curves in Fig. 3(d)), which were roughly consistent with the HE results.

To evaluate the spatiotemporal changes of astrocyte proliferation quantitatively, GFAP+ cells were counted in ROIs of $200 \times 200 \mu\text{m}^2$ in layer 2/3 separately in the IC, CP boundary, and RP areas. The IC region, surrounded by reactive astrocytes and glial scar tissue, contained no GFAP+ astrocytes after Day 3, suggesting a demise of astrocytes. The GFAP+ cell density dropped to zero after Day 1 and did not recover thereafter (see the blue triangle line in Fig. 3(g)). In the CP boundary, the GFAP+ cell density increased continuously until Day 21 after PT (see the blue triangle line in Fig. 3(h)), suggesting astrocyte proliferation in the infarction boundary. In RP, the GFAP+ cell density reached the highest level within 3 days after ischemia and gradually decreased thereafter (see the blue triangle line in Fig. 3(i)). The dynamic changes of cortical astrocytes were significantly correlated to the OAC measurement with Pearson correlation coefficients of 67.4%, 91.3%, and 93.9% in IC, CP, and RP areas, respectively.

3.7. Correlation of OAC mapping with neuronal response to PT by NeuN staining

NeuN+ cells presented a dramatic spatiotemporal change after PT, as shown in Fig. 3(e), and the lower panel of Fig. 3e shows the corresponding enlarged views of the rectangular areas around the damaged tissues. In the baseline before PT, normal neurons were observed with a round and plump morphology in brown (see the hollow arrowheads in the lower panel of Fig. 3(e)), which was consistent with the HE images. On Day 1 after PT, although neurons with round and plump morphology can be observed, NeuN expression (brown) reduced significantly (see Day 1 in the lower panel of Fig. 3(e)). From Day 3 after PT, no brown normal neurons were observed in the

infarction area (see Day 3–21 in the lower panel of Fig. 3(e)), and the solid arrowheads indicate NeuN+ neurons outside the ischemic infarction. According to the NeuN density, experienced experimentalists manually drew the black dotted curves, which were roughly consistent with the HE and GFAP results.

To evaluate the dynamic changes of neurons quantitatively, NeuN+ cells were also counted in the three ROIs, namely the IC, CP, and RP areas, separately. In IC, the density of NeuN+ cells dramatically decreased in the first 3 days after PT and became entirely undetectable in the subsequent days (see the green squared line in Fig. 3(g)). In the CP boundary, a significant reduction in the density of NeuN+ cells was also observed in the first 3 days after PT, following which slight decreases were observed over time (see the green squared line in Fig. 3(h)). In RP, the density of NeuN+ cells decreased in the first 3 days after PT and then increased on Day 14 (see the green squared line in Fig. 3(i)). The dynamic changes in the cortical neurons were significantly correlated to the OAC measurement with Pearson correlation coefficients of -87.0% and -75.5% in the CP boundary and RP areas, respectively. The negative sign indicates that the elevation of OAC might correspond to the death of neurons. In the IC area, a low Pearson correlation coefficient (20.1%) was obtained between the OAC measurement and NeuN+ cell density.

4. Discussion and conclusion

In ischemic stroke, OAC provides important information on the tissue composition, and a thorough understanding of the physiological origin of the OAC contrast would facilitate the appropriate interpretation of OAC results. In this study, multiple approaches were employed to investigate the physiological origin of the OAC contrast. The results suggest that OAC imaging offers non-invasive infarction detection and that its contrast might originate from the changes in astrocytes and neurons in the chronic PT stroke model. By accessing angiogenesis and neurogenesis with OCTA and OAC-OCT, respectively, in a label-free, real-time, and non-invasive manner, OCT can potentially be employed to evaluate the performance of neurorestorative therapy and accelerate the development of novel therapies for chronic stroke.

In this study, fresh *ex vivo* brain slices of PT stroke rat were used to test the feasibility of OAC-based infarction detection. Accordingly, an objective OAC threshold was determined for infarction segmentation. Some differences in the optical properties exist between *ex vivo* and *in vivo* tissues, which might cause OAC differences and threshold deviations between tissues. However, without the ground truth based on histology, it is not suitable to determine the segmentation threshold by using *in vivo* tissues as training data. Therefore, *ex vivo* tissue is generally used as training data for threshold determination, such as the threshold establishment in cancer segmentation [10]. From our results, the OAC was elevated in the infarction area in *ex vivo* tissues, which is consistent with previous studies [3,4]. With a threshold of 0.9 mm^{-1} from *ex vivo* tissues, the OAC-detected infarction and the ischemic area were matched spatially, which further verified the feasibility of threshold determination *ex vivo*. However, a global threshold of 0.90 mm^{-1} was used in this study without considering differences in system noise and individual differences in the experimental animals. In addition, although OCT imaging was completed immediately after (within 5 min) TTC staining to avoid changes in optical properties over time in *ex vivo* tissues [31], the optical properties may change during processing steps such as transcardial perfusion and TTC incubation, the influences of which on the OAC threshold determination deserve further investigation.

With the segmentation threshold, OAC-based infarction detection requires precise OAC measurement with low fluctuations. OAC fluctuations can cause overlaps in OAC distributions between infarction and normal tissues, resulting in segmentation errors. The proposed HDM method was more effective in reducing the segmentation error compared to the conventional spatial averaging method. Compared with the spatial averaging method, sub-samples in the

HDM method were more independent with a lower correlation coefficient [32], providing a better smoothing effect. Although splitting the wavelength spectrum and the full-space B-scan modulation spectrum would degrade the spatial resolution, which is a limitation of the spatial averaging method as well, a light source with wider bands and higher numerical aperture can be adopted to reduce the resolution degradation. In this study, a kernel size of 5 by 5 was empirically selected after considering the tradeoff between the OAC precision improvement and spatial-resolution degradation. According to the tissue phantom experiments, the HDM method shows a minimal reduction (less than 7%) in the measured OAC values, and a possible reason for this reduction is that the sub-spectrums distant to the center have extremely low intensity. The light with insufficient intensity is attenuated to the noise level immediately after penetrating the tissue surface and the flat noise floor corresponds to a low OAC estimate. In the present study, the spectrum was split with an equational bandwidth, which should be optimized in future studies. With the correlation between OAC changes and tissue injury, the HDM method can be used not only in the infarction detection in stroke, but also in the detection of brain cancer [10], atherosclerosis [11], and skin burn scars [22]. In the HDM method, repeated B-frames were not conducted to avoid the disturbance of time averaging. There is a high correlation coefficient (77.2%) between repeated B-frames, which makes time averaging contributed less to OAC measurement improvement. Although the effect of time averaging is limited, repeated B-frames for time averaging can be also conducted in the practical application.

In the chronic phase of ischemic stroke, our results suggest that OAC elevation is spatiotemporally correlated to astrocytic changes positively and neuronal responses negatively in the PT stroke model. Attenuation is caused by both scattering and absorption. For the wavelength of 1325 nm selected in this study, light absorption is negligible in comparison to the scattering in tissue. OAC was mainly affected by the scattering properties, which are mainly dependent on the cellular morphology and functions [33]. The molecular and cellular events after ischemia are characterized by reactive astrocytes with enhanced GFAP expression in the penumbra, which eventually form glial scar tissue surrounding the infarction in the chronic phase (see Fig. 3(d)) [34]. In the CP boundary, OAC was elevated continuously along with the formation of glial scarring, which suggested that the elevated OAC might correspond to the increase of astrocytes and the death of neurons. Notably, liquefactive necrosis occurs in the IC region, where it is transformed into a liquid viscous mass and forms a stroke cavity in the weeks subsequent to stroke [35], which might not induce OAC elevation. Owing to the tightly coupled responses of astrocytes and neurons in ischemic stroke, independent analyses of the OAC–astrocyte and OAC–neuron correlation were not conducted in the current study. In addition, brain edema and swelling have been observed with histochemistry and magnetic resonance imaging after PT ischemia, and they reached the maximum 1–3 days after PT [34]. However, the accumulation of excess fluid in the edema induced a decrease in OAC in the cerebral cortex [36] and thus should not be the primary contribution to the elevation of OAC.

In addition to the chronic phase, the present study sheds light on the acute phase. Compared with the baseline, apoptotic neurons with condensed nuclei (see the solid arrows in Fig. 3(c)) and edema with widened intercellular spaces (see the hollow arrows in Fig. 3(c)) were observed 1 h after PT, and NeuN expression (brown) was significantly reduced. These observations support the hypothesis that the increased OAC was mainly caused by cell damage and cell necrosis [5,6].

Funding

Zhejiang Provincial Natural Science Foundation of China (LR19F050002); Zhejiang Lab (2018EB0ZX01); Fundamental Research Funds for the Central Universities (2018FZA5003); National Natural Science Foundation of China (81873911).

Disclosures

P.L., K.X., and S.Y. conceived and designed the study. P.L. and S.Y. designed and built the system. K.X., K.Z.L., and G.W. prepared the animals. P.L., and S.Y. analyzed the data. P.L., K.X., S.Y., K.Z.L., L.Y., and K.Y.L. wrote the manuscript. The authors declare that there are no conflicts of interest related to this article.

References

1. C. Stapf and J. P. Mohr, "Ischemic Stroke Therapy," *Annu. Rev. Med.* **53**(1), 453–475 (2002).
2. V. J. Srinivasan, E. T. Mandeville, A. Can, F. Blasi, M. Climov, A. Daneshmand, J. H. Lee, E. Yu, H. Radhakrishnan, E. H. Lo, S. Sakadzic, K. Eikermann-Haerter, and C. Ayata, "Multiparametric, longitudinal optical coherence tomography imaging reveals acute injury and chronic recovery in experimental ischemic stroke," *PLoS One* **8**(8), e71478 (2013).
3. U. Baran, Y. Li, and R. K. Wang, "In vivo tissue injury mapping using optical coherence tomography based methods," *Appl. Opt.* **54**(21), 6448–6453 (2015).
4. Y. Li, W. J. Choi, W. Qin, U. Baran, L. M. Habenicht, and R. K. Wang, "Optical coherence tomography based microangiography provides an ability to longitudinally image arteriogenesis in vivo," *J. Neurosci. Methods* **274**, 164–171 (2016).
5. W. J. Choi, Y. Li, and R. K. Wang, "Monitoring Acute Stroke Progression: Multi-Parametric OCT Imaging of Cortical Perfusion, Flow, and Tissue Scattering in a Mouse Model of Permanent Focal Ischemia," *IEEE Trans. Med. Imag.* **38**(6), 1427–1437 (2019).
6. S. Yang, K. Liu, H. Ding, H. Gao, X. Zheng, Z. Ding, K. Xu, and P. Li, "Longitudinal in vivo intrinsic optical imaging of cortical blood perfusion and tissue damage in focal photothrombosis stroke model," *J. Cereb. Blood Flow Metab.* **39**(7), 1381–1393 (2019).
7. J. Liu, N. Ding, Y. Yu, X. Yuan, S. Luo, J. Luan, Y. Zhao, Y. Wang, and Z. Ma, "Optimized depth-resolved estimation to measure optical attenuation coefficients from optical coherence tomography and its application in cerebral damage determination," *J. Biomed. Opt.* **24**(3), 1–11 (2019).
8. L. Thrane, M. H. Frosz, T. M. Jorgensen, A. Tycho, H. T. Yura, and P. E. Andersen, "Extraction of optical scattering parameters and attenuation compensation in optical coherence tomography images of multilayered tissue structures," *Opt. Lett.* **29**(14), 1641–1643 (2004).
9. D. J. Faber, F. J. V. D. Meer, and M. C. G. Aalders, "Quantitative measurement of attenuation coefficients of weakly scattering media using optical coherence tomography," *Opt. Express* **12**(19), 4353 (2004).
10. C. Kut, K. L. Chaichana, J. Xi, S. M. Raza, X. Ye, E. R. McVeigh, F. J. Rodriguez, A. Quiñones-Hinojosa, and X. Li, "Detection of human brain cancer infiltration ex vivo and in vivo using quantitative optical coherence tomography," *Sci. Transl. Med.* **7**(292), 292ra100 (2015).
11. C. Xu, J. M. Schmitt, S. G. Carlier, and R. Virman, "Characterization of atherosclerosis plaques by measuring both backscattering and attenuation coefficients in optical coherence tomography," *J. Biomed. Opt.* **13**(3), 8 (2008).
12. K. A. Vermeer, J. Mo, J. J. Weda, H. G. Lemij, and J. F. de Boer, "Depth-resolved model-based reconstruction of attenuation coefficients in optical coherence tomography," *Biomed. Opt. Express* **5**(1), 322–337 (2014).
13. K. A. Vermeer, J. van der Schoot, H. G. Lemij, and J. F. de Boer, "Quantitative RNFL attenuation coefficient measurements by RPE-normalized OCT data," 8209, 82090U (2012).
14. R. Kafieh, H. Rabbani, and S. Kermani, "A review of algorithms for segmentation of optical coherence tomography from retina," *J. Med. Signals Sens.* **3**(1), 45–60 (2013).
15. K. Qin, K. Xu, F. Liu, and D. Li, "Image segmentation based on histogram analysis utilizing the cloud model," *Comput. Math. Appl.* **62**(7), 2824–2833 (2011).
16. F. J. V. D. Meer, J. Perree, D. J. Faber, D. M. B. Sassoon, M. C. G. Aalders, and T. G. V. Leeuwen, Discrimination of atherosclerotic plaque constituents based on local measurements of optical attenuation coefficients by OCT, SPIE BiOS (SPIE, 2005), Vol. 5686.
17. J. C. Grotta, W. S. Burgin, A. El-Mitwalli, M. Long, M. Campbell, L. B. Morgenstern, M. Malkoff, and A. V. Alexandrov, "Intravenous Tissue-Type Plasminogen Activator Therapy for Ischemic Stroke: Houston Experience 1996 to 2000," *Arch. Neurol.* **58**(12), 2009–2013 (2001).
18. J. Chen and M. Chopp, "Neurorestorative treatment of stroke: cell and pharmacological approaches," *NeuroRx* **3**(4), 466–473 (2006).
19. J. Chen, P. Venkat, A. Zacharek, and M. Chopp, "Neurorestorative therapy for stroke," *Front. Hum. Neurosci.* **8**, 382 (2014).
20. H. Wang, C. Magnain, S. Sakadžić, B. Fischl, and D. A. Boas, "Characterizing the optical properties of human brain tissue with high numerical aperture optical coherence tomography," *Biomed. Opt. Express* **8**(12), 5617–5636 (2017).
21. P. Li, Y. Cheng, P. Li, L. Zhou, Z. Ding, Y. Ni, and C. Pan, "Hybrid averaging offers high-flow contrast by cost apportionment among imaging time, axial, and lateral resolution in optical coherence tomography angiography," *Opt. Lett.* **41**(17), 3944–3947 (2016).

22. P. Li, Y. Cheng, L. Zhou, C. Pan, Z. Ding, and P. Li, "Single-shot angular compounded optical coherence tomography angiography by splitting full-space B-scan modulation spectrum for flow contrast enhancement," *Opt. Lett.* **41**(5), 1058–1061 (2016).
23. L. Huang, Y. Fu, R. Chen, S. Yang, H. Qiu, X. Wu, S. Zhao, Y. Gu, and P. Li, "SNR-adaptive OCT angiography enabled by statistical characterization of intensity and decorrelation with multi-variate time series model," *IEEE Trans. Med. Imag.* **38**(11), 2695–2704 (2019).
24. F. Zhang and J. Chen, "Infarct Measurement in Focal Cerebral Ischemia: TTC Staining," in *Animal Models of Acute Neurological Injuries II: Injury and Mechanistic Assessments*, Volume 2, J. Chen, X.-M. Xu, Z. C. Xu, and J. H. Zhang, eds. (Humana Press, Totowa, NJ, 2012), pp. 93–98.
25. W. Zhang, Y. Xie, T. Wang, B. Jing, H. Li, Q. Z. Li, Q. Y. Shui, and S. Ding, "Neuronal protective role of PBEF in a mouse model of cerebral ischemia," *J. Cereb. Blood Flow Metab.* **30**(12), 1962–1971 (2010).
26. S. Watanabe, J. R. Hoffman, R. L. Craik, P. J. Hand, S. E. Croul, M. Reivich, and J. H. Greenberg, "A new model of localized ischemia in rat somatosensory cortex produced by cortical compression," *Stroke* **32**(11), 2615–2623 (2001).
27. J. Defelipe, "The evolution of the brain, the human nature of cortical circuits, and intellectual creativity," *Front. Neuroanat.* **5**, 29 (2011).
28. D. Lanjakornsiripan, B. J. Pior, D. Kawaguchi, S. Furutachi, T. Tahara, Y. Katsuyama, Y. Suzuki, Y. Fukazawa, and Y. Gotoh, "Layer-specific morphological and molecular differences in neocortical astrocytes and their dependence on neuronal layers," *Nat. Commun.* **9**(1), 1623 (2018).
29. A. Saraste and K. Pulkki, "Morphologic and biochemical hallmarks of apoptosis," *Cardiovasc. Res.* **45**(3), 528–537 (2000).
30. H. Lu and X. Lei, "The apparent diffusion coefficient does not reflect cytotoxic edema on the uninjured side after traumatic brain injury," *Neural Regener. Res.* **9**(9), 973–977 (2014).
31. E. B. Kiseleva, Y. V. Korzhimanova, A. A. Moiseev, K. S. Yashin, L. B. Timofeeva, G. V. Gelikonov, E. V. Zagaynova, and N. D. Gladkova, "Time-related ex vivo changes in the optical properties of normal brain tissues," *Laser Phys. Lett.* **16**(4), 045602 (2019).
32. P. Li, Y. Cheng, P. Li, L. Zhou, Z. Ding, Y. Ni, and C. Pan, "Hybrid averaging offers high-flow contrast by cost apportionment among imaging time, axial, and lateral resolution in optical coherence tomography angiography," *Opt. Lett.* **41**(17), 3944–3947 (2016).
33. R. Drezek, A. Dunn, and R. Richards-Kortum, "Light scattering from cells: finite-difference time-domain simulations and goniometric measurements," *Appl. Opt.* **38**(16), 3651–3661 (1999).
34. H. Li, N. Zhang, H. Lin, Y. Yu, Q. Cai, L. Ma, and S. Ding, "Histological, cellular and behavioral assessments of stroke outcomes after photothrombosis-induced ischemia in adult mice," *BMC Neurosci.* **15**(1), 13 (2014).
35. A. Hong, M.-I. Aguilar, M. P. Del Borgo, C. G. Sobey, B. R. S. Broughton, and J. S. Forsythe, "Self-assembling injectable peptide hydrogels for emerging treatment of ischemic stroke," *J. Mater. Chem. B* **7**(25), 3927–3943 (2019).
36. C. L. Rodriguez, J. I. Szu, M. M. Eberle, Y. Wang, M. S. Hsu, D. K. Binder, and B. H. Park, "Decreased light attenuation in cerebral cortex during cerebral edema detected using optical coherence tomography," *Neurophotonics* **1**(2), 025004 (2014).